Università degli Studi di Padova

Dipartimento di Ingegneria Industriale DII

Corso di Laurea Magistrale in Ingegneria Aerospaziale

NUMERICAL INVESTIGATION OF HIGH SPEED PROPELLER UNDER BOUNDARY LAYER INGESTION CONDITIONS

Relatore: Prof. Andrea Magrini
Correlatore: Ing. Manuel Casablanca

Laureando: Simone Marchesani, 2095754

Anno Accademico 2024/2025

Ai miei genitori, che mi hanno sempre sostenuto e supportato nei momenti di difficoltà e hanno incoraggiato ogni mia scelta. Ai miei nonni, fonte inesauribile di saggezza e dolcezza.
E infine a te, che con me non hai mai mollato, donandomi forza e motivazione nei momenti difficili.
Grazie a tutti voi.

ABSTRACT

Turboprop engines are generally characterized by high efficiency at medium-to-low cruise speeds, but this efficiency significantly decreases as the flight Mach number increases. While these engines perform effectively in subsonic regimes, their efficiency drops sharply in supersonic conditions. In the 1970s, NASA launched the Advanced Turboprop Program (ATP) [1], aiming to develop transonic propellers capable of overcoming these limitations. One such propeller is the SR2, which is the focus of this thesis. This work primarily focuses on validating the data provided by NASA in its scientific publications, followed by an analysis of the propeller's performance in a boundary layer ingestion (BLI) condition, i.e., when installed behind the fuselage, where it ingests the airframe boundary layer. Specifically, key performance coefficients, such as the thrust coefficient, power coefficient, and efficiency, were examined for both the BLI configuration and a conventional propeller setup. The results obtained indicate that the BLI configuration offers superior performance compared to the conventional configuration in several aspects. In particular, the BLI configuration achieves a maximum efficiency of approximately 91%, while the conventional configuration reaches a maximum of about 79%.

Sommario

I motori turboelica sono generalmente caratterizzati da un'elevata efficienza a velocità di crociera medio-basse, ma questa efficienza diminuisce significativamente con l'aumentare del numero di Mach di volo. Sebbene questi motori operino efficacemente in regimi subsonici, la loro efficienza cala drasticamente in condizioni supersoniche. Negli anni '70, la NASA ha avviato il Advanced Turboprop Program (ATP) [1], con l'obiettivo di sviluppare eliche transoniche in grado di superare queste limitazioni. Una di queste eliche è la SR2, che è l'oggetto di studio di questa tesi. Questo lavoro si concentra principalmente sulla validazione dei dati forniti dalla NASA nelle sue pubblicazioni scientifiche, seguita da un'analisi delle prestazioni dell'elica in condizioni di boundary layer ingestion (BLI), ovvero quando è installata dietro la fusoliera, dove ingerisce lo strato limite generato dalla cellula. In particolare, sono stati esaminati i principali coefficienti prestazionali, come il coefficiente di spinta, il coefficiente di potenza e l'efficienza, sia per la configurazione BLI che per una configurazione convenzionale dell'elica. I risultati ottenuti indicano che la configurazione BLI offre prestazioni superiori rispetto alla configurazione convenzionale in diversi aspetti. In particolare, la configurazione BLI raggiunge un'efficienza massima di circa il 91%, mentre la configurazione convenzionale arriva a un massimo di circa il 79%.

CONTENTS

List of Figures

List of Tables

Abbreviations

ATP Avanced Turboprop Projects.

BEMT Blade Element Momentum Theory.

BLI Boundary Layer Ingestion.

CP Conventional Propeller.

MRF Multiple Reference Frame.

RANS Reynold Average Navier-Stokes.

SFC Specific Fuel Consumption.

SST Shear Stress Transport.

Nomenclature

C_q Torque Coefficient.

C_t Thrust Coefficient.

C_w Power Coefficient.

V_∞ Free stream velocity.

α angle of attack.

β Blade Pitch Angle.

η Propeller efficiency.

h Flight Altitude.

B Number of Blades.

c Blade Chord.

D Propeller diameter.

J Advance Ratio.

M Flight Mach Number.

n Propeller Speed Rotation in rev/s.

Q Torque.

r Propeller radius.

s Propeller span.

1 INTRODUCTION

In this chapter, we introduce the fundamentals of propellers, including the key coefficients that describe their performance, operating principles, and characteristics. We then discuss the unique features of the SR2 propeller, which is the focus of this thesis.

A propeller is a device that converts mechanical energy into thrust, which propels the vehicle to which it is attached. Propellers generate a small acceleration over a large mass of air. However, their drawback is that they are typically confined to low subsonic applications. NASA has addressed this issue through its ATP program [1], aiming to develop propellers that maintain high efficiency even at high Mach numbers. The NASA SR2 propeller is one of the designs developed within this program.

1.1 Propeller Overview

1.1.1 Propeller Performance

The conventional propellers installed in turboprop engines can achieve a maximum efficiency of $\eta = 80\%$ at approximately Mach M = 0.5/0.6. However, beyond this Mach number, they experience a drop in efficiency [2], as shown in 1.2a. This drop is due to the compressibility effects that occur near the tip of the blade when $M \approx 1$. This limitation is partially addressed by the propfan, which, thanks to its advanced blade shape, can delay compressibility effects and maintain high performance, at least up to $M = 0.8$. One of the biggest issues with propfans is the noise they generate.

(a) Leonardo ATR-42 Turboprop

(b) AGE-36 propfan on Mc Douglass

Figure 1.1: Examples of Turboprop and Propfan engine

Figure 1.2b compares the Specific Fuel Consumption with the Mach Flight number. It is clear that the turboprop has the lowest fuel consumption among the different engines, but it increases rapidly when $M = 0.5/0.6$ is reached. For the advanced turboprop (Propfan), the rise is delayed until $M = 0.7/0.8$.

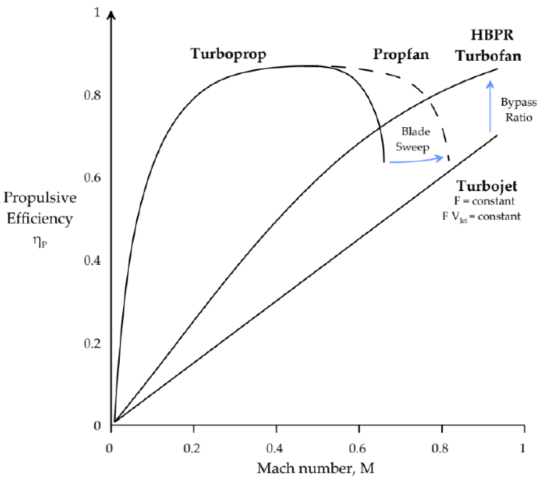

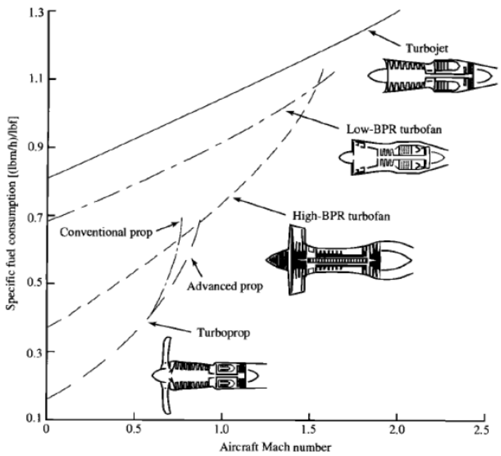

(a) Efficiency vs Flight Mach number

(b) SFC vs Flicht Mach number

Figure 1.2: Efficiency and SFC vs Flicht Mach number [2]

1.1.2 CP and BLI Propeller

In this thesis, we analyze two types of propeller configurations: Conventional Propeller (CP) and the propeller with Boundary Layer Ingestion (BLI). In figure1.3, the main difference can be observed: in the conventional propeller case (a), the propeller operates using undisturbed and clean airflow, whereas in the BLI case (b), the propulsion system is positioned at the aft of the fuselage, ingesting the airframe boundary layer. The main benefit of this configuration is the re-energization of the boundary layer flow, which has a lower velocity than the freestream velocity. This results in higher efficiency and, consequently, greater fuel savings. The conventional propeller accelerate the freestream velocity from V_∞ to a jet velocity V_j. For an ideal case the thrust exhausted is:

$$T_{CP} = \dot{m}(V_j - V_\infty) \tag{1.1}$$

The power W_{conv} given to the flow by the propeller is equal to the difference between the inflow and outflow kinetic energy:

$$W_{CP} = \frac{\dot{m}}{2}(V_j^2 - V_\infty^2) = \frac{T_{cp}}{2}(V_j - V_\infty) \tag{1.2}$$

However, the BLI propeller experiments the boundary layer velocity V_w which is lower than the freestream velocity ($V_w < V_\infty$. The thrust exhausted is:

$$T_{BLI} = \dot{m}(V_w - V_{j-BLI}) \tag{1.3}$$

In the same fashion as the $W_C P$:

$$W_{BLI} = \frac{\dot{m}}{2}(V_{j-BLI}^2 - V_w^2) = \frac{T_{BLI}}{2}(V_{j-BLI} - V_w) \tag{1.4}$$

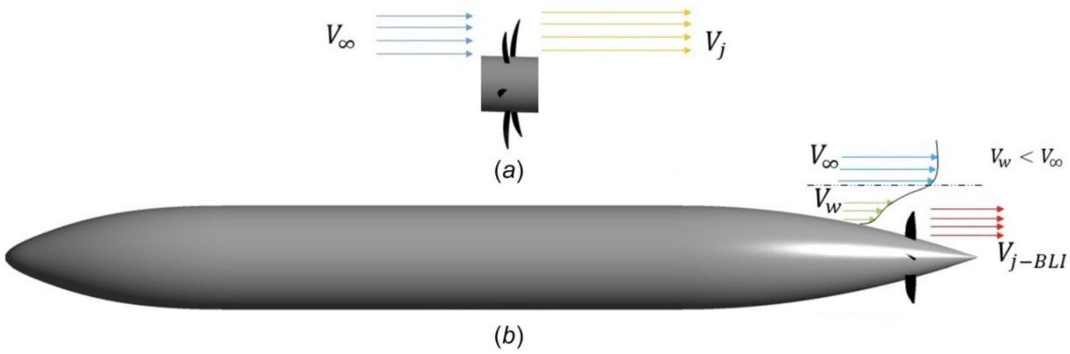

Figure 1.3: Difference from CP (a) and BLI (b) propeller [3]

Assuming constant mass flow $\dot{m}$ for both CP and BLI propeller and also that they produce the exhaust the same thrust $T_{CP} = T_{BLI}$. Comparing eqs. 1.2 and 1.4 it is possible to see that, for a given propeller force, less power needs to be added to the flow in the BLI case. This is the reason why BLI allows the engine to reduce fuel consumption compared to the CP case.

1.2 Propeller Basics

In figure 1.4 it is possible to observe a typical section of a generic propeller: it is usually be described as a twisted stack of different airfoil from the hub to the tip.

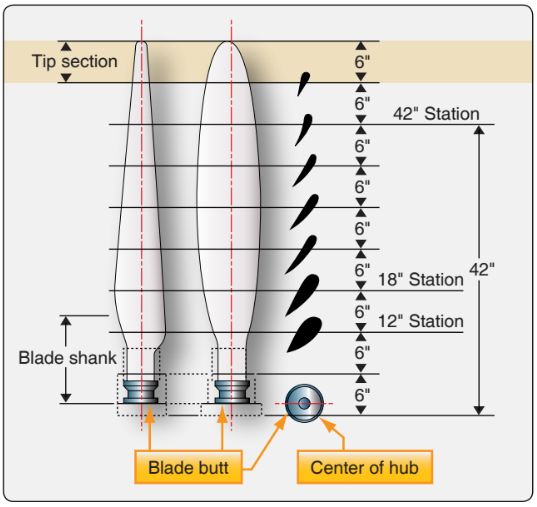

Figure 1.4: Typical propeller blade elements[4]

There are two main types of propellers:

- **Fixed Pitch**: The blades are rigidly attached to the hub at a fixed angle, which cannot be adjusted during flight. The pitch angle is predetermined by the manufacturer based on the expected operating conditions. Fixed-pitch propellers are simple, lightweight, and cost-effective, but they offer limited efficiency across different flight phases.

- **Variable Pitch**: In this case, the blades are not fixed to the hub but can rotate around their own axis, allowing the pitch angle to change during flight. This variability improves performance by optimizing thrust and efficiency at different speeds and altitudes[5]. Variable-pitch propellers are commonly used in high-performance aircraft and can include constant-speed mechanisms to maintain optimal RPM automatically.

Unlike a fixed wing, a propeller experiences a more complex aerodynamic environment due to its rotational motion, which significantly alters the direction and magnitude of the relative airflow across the blades. In figure 1.5 we show the flow seen from a rotating blade:

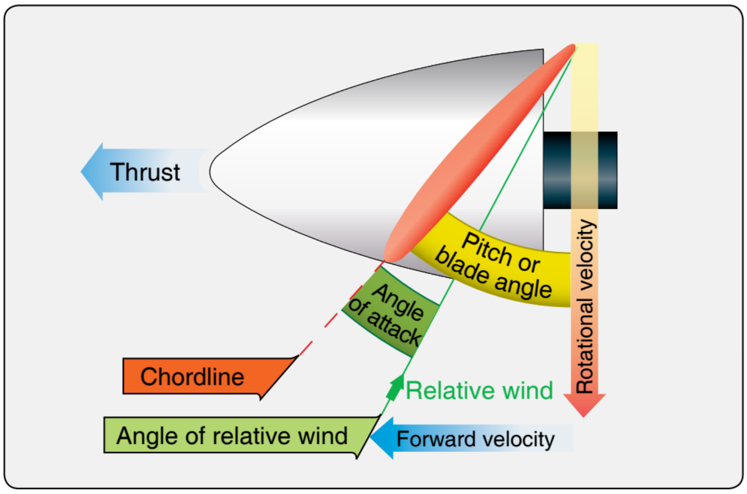

Figure 1.5: Airflow seen from a rotating Blade

In fact, the relative wind is given by the vector sum of the rotational velocity and the forward velocity:

$$\vec{V}_{\text{rel}} = \vec{V}_{\text{forward}} + \vec{\omega} \times \vec{r} \tag{1.5}$$

Thus, the angle of attack α is defined in the same way as for a fixed wing, namely as the angle between the relative wind and the chord of the airfoil. However, since the spanwise position r varies from the hub to the tip of the blade, the relative velocity also changes along the span,from equation 1.5 a variations in the angle of attack is induced. As shown in figure 1.5 the β pitch angle is the angle between the plane of the propeller rotation and the chordline.

1.3 Main Propeller Parameters

In this section, we will introduce the main propeller parameters that will be analyzed in this thesis. The key parameters are:

- Thrust Coefficient:
$$C_T = \frac{T}{\rho n^2 D^4} \tag{1.6}$$
- Power Coefficient:
$$C_w = \frac{W}{\rho n^3 D^5} \tag{1.7}$$
- Torque Coefficient:
$$C_q = \frac{Q}{\rho n^2 D^5} \tag{1.8}$$
- Advance Ratio:
$$J = \frac{V_\infty}{nD} \tag{1.9}$$
- Efficiency
$$\eta = J\frac{C_t}{C_p} \tag{1.10}$$

From Equation 1.9 and Figure 1.5, it is clear that J is linked to the blade pitch angle β and their relationship is shown in Equation 1.11.

$$\alpha = \beta - arctan(J) \tag{1.11}$$

So, efficiency η is heavily influenced by the combination between J and β, and this is shown is graph 1.6:

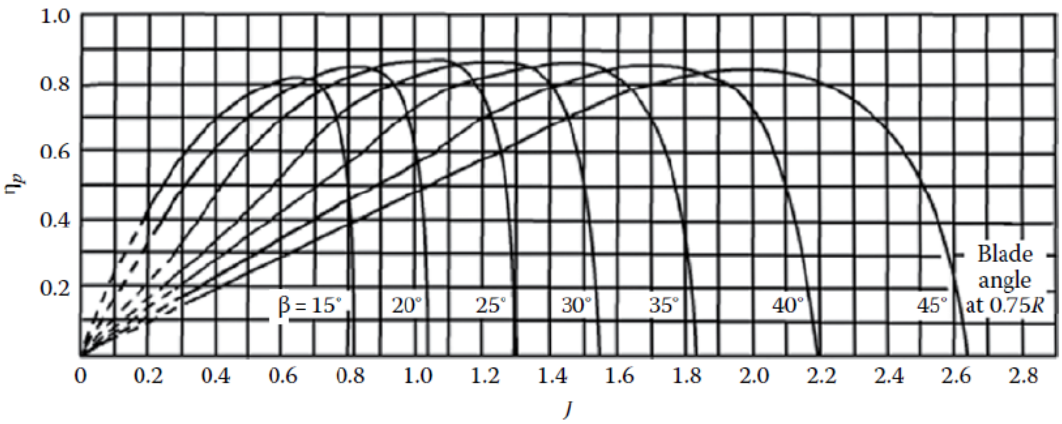

Figure 1.6: Efficiency vs J for a generic Propeller

Figure 1.6 highlights the importance of the pitch angle for a propeller. If a propeller can adjust this angle, it becomes possible to change the cruise velocity while maintaining maximum efficiency. In fact, according to equation 1.9, if the freestream velocity V_∞ changes, the advance ratio J also changes. If the blade pitch angle β remains constant, the efficiency η drops rapidly.

1.4 About SR2 Propeller

In this final introduction section, we will introduce the main characteristics of the NASA SR2 propeller. Figure 1.7 shows the model used by NASA to study its aerodynamic properties, and Table 1.1 presents its key characteristics.

Figure 1.7: SR2 propeller model inside NASA wind tunnel

Parameter	Value
Diameter [cm]	62.2
Number of blades B	8
Design Mach number	0.80
Design tip speed [m/s]	244
Design advance ratio	3.06
Design power coefficient	1.7
Design power loading [kW/m^2]	301
Activity factor	203
Blade setting angle [deg]	56.7

Table 1.1: Propeller Design Parameters

2 Materials and Methods

In this chapter, we present the fundamental theoretical concepts behind airfoil design and describe the specific airfoils that make up the SR2 propeller. We explain how we construct the blade geometry using NASA's reference data and show the steps we follow to process and refine this data. We ensure accuracy and consistency in the representation of the airfoil sections. We also describe how we generate the CAD model of the NASA SR2 propeller and highlight the main challenges we encounter. We present the solutions we adopt to overcome these challenges. Finally, we show how we build the computational mesh and describe the complete model used for the analyses. We explain the techniques we apply to create a high-quality mesh that accurately represents the propeller geometry while ensuring numerical stability and efficiency. We also illustrate how we set up the computational domain and define the boundary conditions that characterize the operating environment of the propeller. We provide a detailed explanation of how these conditions influence the simulation results and ensure that they correctly replicate the real aerodynamic behavior of the propeller.

2.1 Airfoil Fundamentals and Blade design

To facilitate a better understanding of the following discussion, it is essential to first familiarize oneself with airfoil terminology and introduce its key parameters. In figure 2.1 is shown a generic airfoil section:

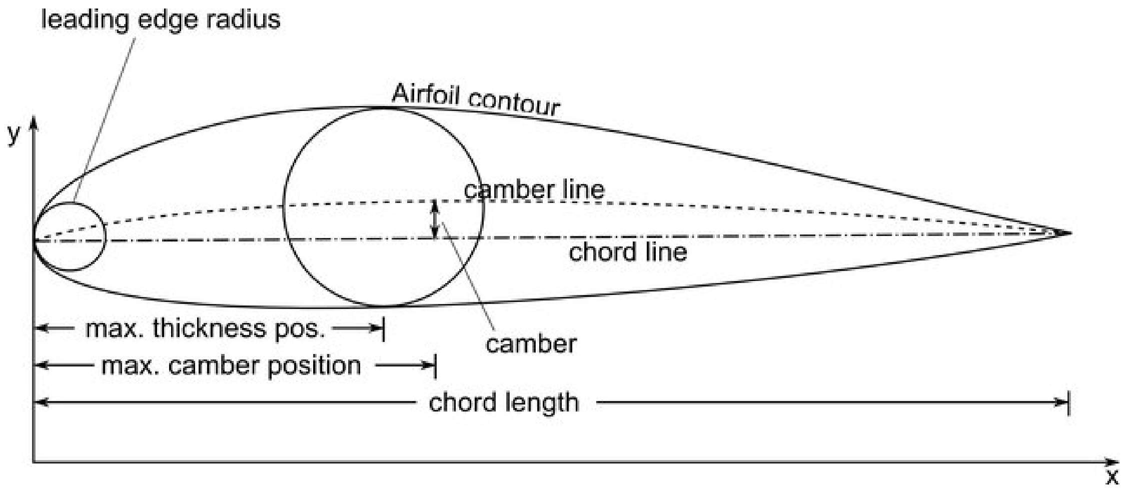

Figure 2.1: Main Parameters of a generic Airfoil

- Leading Edge (LE) : is the part of the airfoil that first contacts the air.
- Trailing Edge (TE) : it is the rear edge of the airfoil, which is the last part that last contacts the air.
- Chord line (C): it is the straight line between the LE and the TE.
- Camber Line : it is to the curve that represents the mean shape of the airfoil's cross-section
- Maxim Thickness : it is the maximum distance from measured between the pressure side and the suctions side.

2.2 Propeller assembly

Once that the basics of airfoil are introduced, we begin to build the blade: the first step is to determine the shape of the Hub and which airfoils constitute the propeller.

2.2.1 Hub Identification

The first step is to identify the coordinates and shape of the hub on which the blade rests. To obtain this information, we can refer to Figure 2.2.

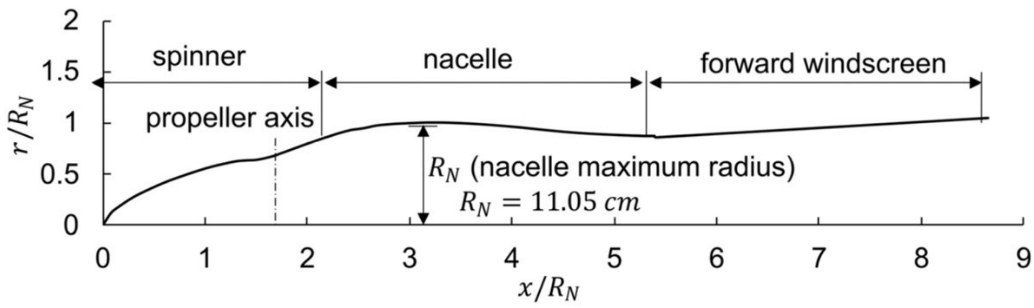

Figure 2.2: SR2 Hub, Nacelle and spinner

Using *Web Plot Digitizer* [6], we scan the figure below to extract the coordinates of the hub. By revolving these coordinates around the z-axis, we can easily obtain the 3D model of the spinner, hub, and nacelle.

2.2.2 Airfoil identification

Thanks Nasa Technical Memorandum [7] is possible to get the propeller characteristics, in particular:

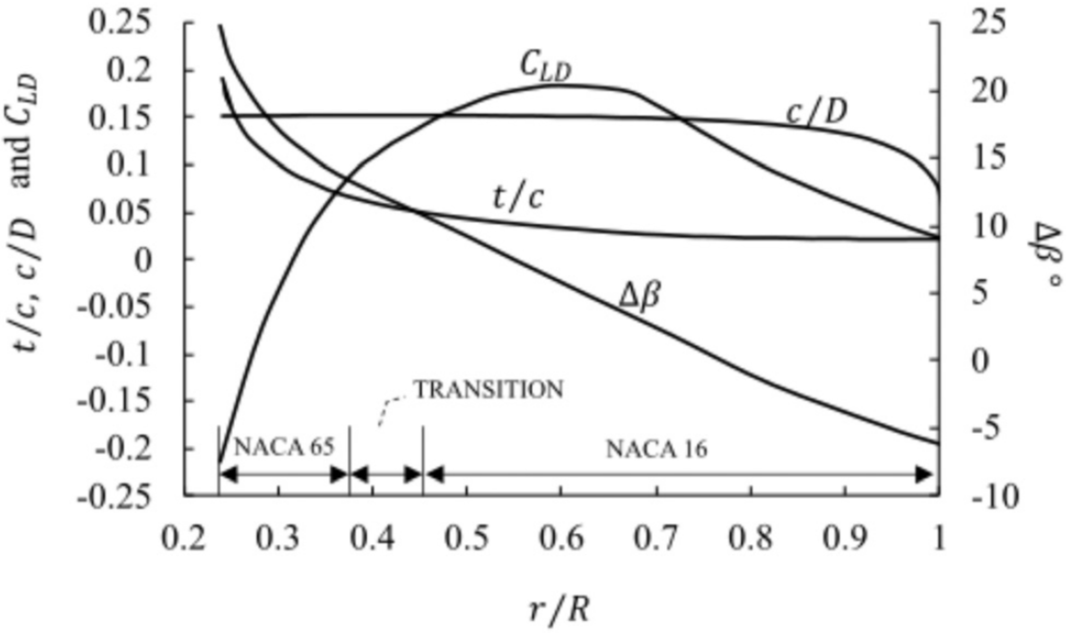

Figure 2.3: SR2 Configuration

From the graph 2.3 is possible to get some fundamentals information:

- **Airfoil type**: The blade is composed of different airfoil series along its span. Specifically, from the root up to approximately 0.37R–0.38R, it consists of NACA 65-series airfoils[8], whereas from 0.45R to the tip, it transitions to NACA 16-series airfoils. However, no information is available regarding the transition region between 0.37R and 0.45R.
- **Thickness-to-chord ratio** (t/c): From the curve, we observe that at the root, this ratio is 0.2, while at the tip, it decreases to 0.02. This indicates that the airfoils near the tip are extremely thin.

- **Pitch angle**: In the graph, $\Delta\beta°$ represents the difference between the pitch angle at a given spanwise location and the pitch angle at $\frac{3}{4}s$ which is by project $\beta_{\frac{3}{4}} = 56.7°$.

We can now begin creating the blade. First, we selected 11 airfoils to discretize it. This number was chosen because it preserves sufficient detail without being too high, which would overly complicate the calculations. Then, we extract the data of graph 2.3 thanks to the free open source *Web Plot Digitizer* [6], interpolating the data thanks to a spline to reduce errors. At this point we determine the pitch angle of each of the 11 airfoil, and it is possible to get it from the $\Delta\beta°$ of the graph and the known value of the pitch angle at $\beta_{\frac{3}{4}}$. We get 2.4

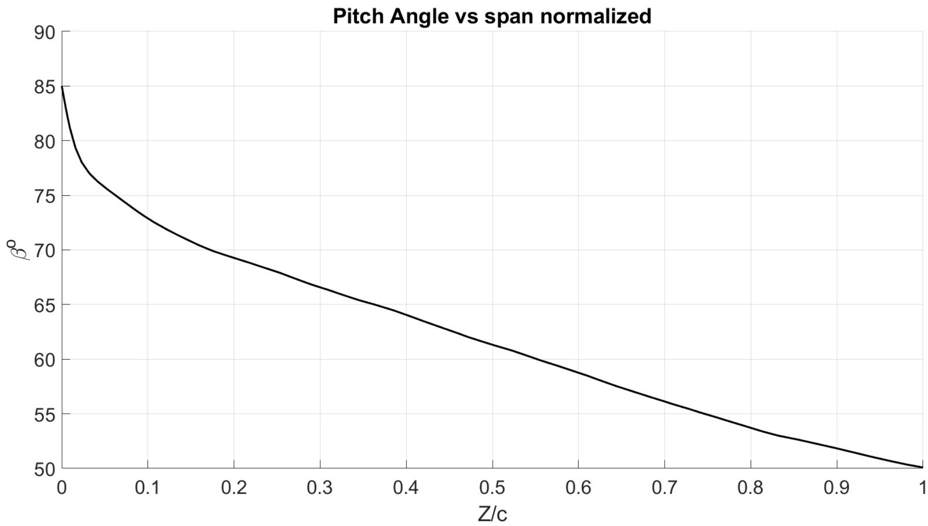

Figure 2.4: Pitch angle for blade Airfoils

At this point, using $\beta, t/c$ and and C_{ld} a first attempt of a 2D airfoil is generated. Then, we create a polar using the open-source software *XFoil* [9], a panel-based CFD tool. Finally, using a BEMT code, we compare our polars with those of NASA. The best airfoil is the one whose polar is as close as possible to NASA's. The final Airfoil set we get is 2.1.

Airfoil	Span
NACA 654221	0
NACA 65007	0.07
NACA 65107	0.13
NACA 16106	0.2
NACA 16205	0.33
NACA 16204	0.467
NACA 16203	0.6
NACA 16202	0.733
NACA 16202	0.827
NACA 16202	0.92
NACA 16202	1

Table 2.1: Airfoil that made up the SR2 Blade

2.2.3 Airfoil 3D coordinates

Once we obtain our 2D airfoil, we need to rotate it clockwise around its centroid by the assigned pitch angle.

Next, we need to stack all these 2D airfoils along a line that passes through the centroid of each airfoil. This line runs along the y-axis.

Now, we must define the final 3D coordinate system of our propeller:

- The blades rotate around the z-axis, which is positive in the direction from the nose of the spinner towards the back of the propeller.
- The y-axis is oriented along the blade, from the hub to the tip.
- The x-axis completes the right-hand rule.

At this point to get the 3D coordinates of the airfoil. To doing so we have to introduce the equations 2.1 and 2.2 We define a curvilinear streamline

$$l = \int_0^z \sqrt{1 + \left(\frac{dr}{dz}\right)^2}\, dz \tag{2.1}$$

$$r(z) = R_{\text{hub}}(z) + s \cdot (R_{\text{tip}} - R_{\text{hub}}(z)) \tag{2.2}$$

Now, it is possible to obtain the l coordinates of the 2D airfoil, and the we can convert it into a z coordinates thanks to equation 2.2. Finally, we can get the coordinates of the 3D airfoil:

$$y_{3D} = r(z)\cos\theta \tag{2.3}$$

$$x_{3D} = r(z)\sin\theta \tag{2.4}$$

$$\theta = atan\frac{y_{2D}}{r(z)} \tag{2.5}$$

In figure 2.7 and 2.8 we show the final results.

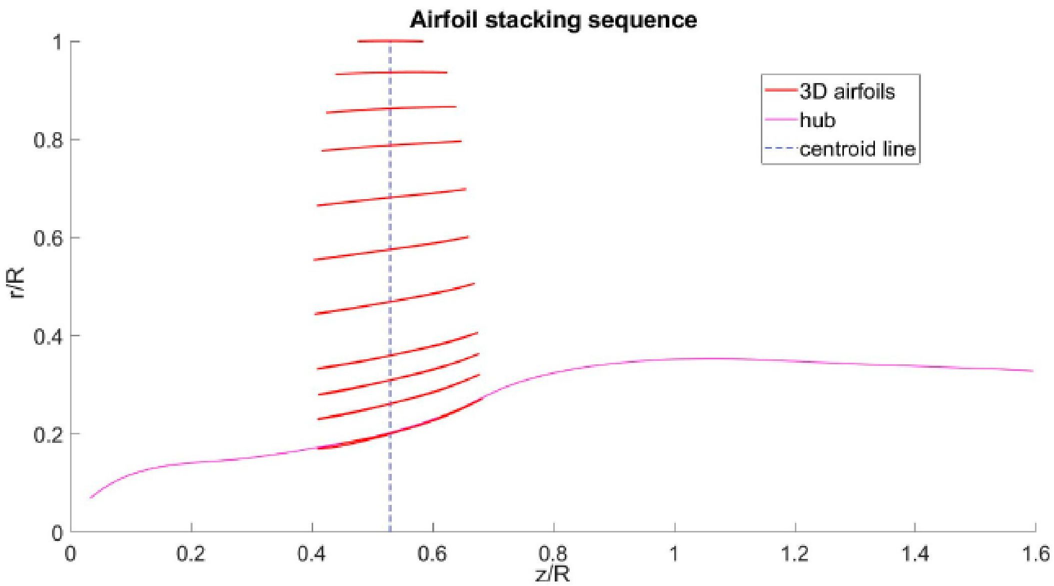

Figure 2.5: Airfoil stack side view

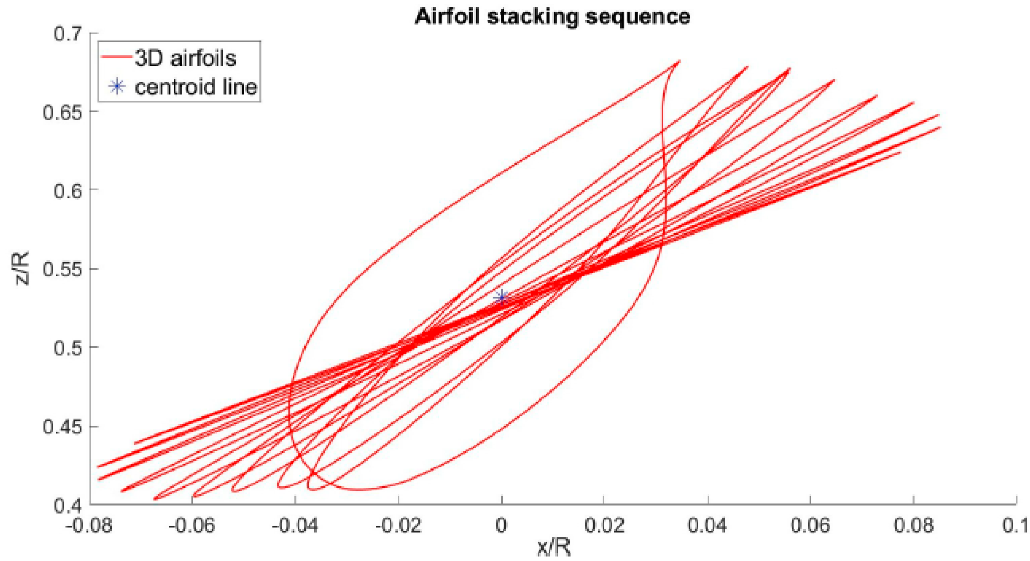

Figure 2.6: Airfoil stack top view

Finally, we can import the coordinate in a 3D software CAD like SolidWorks[10] and we can create our blade. In figure 2.7 and 2.8 we show the final SR2 propeller model.

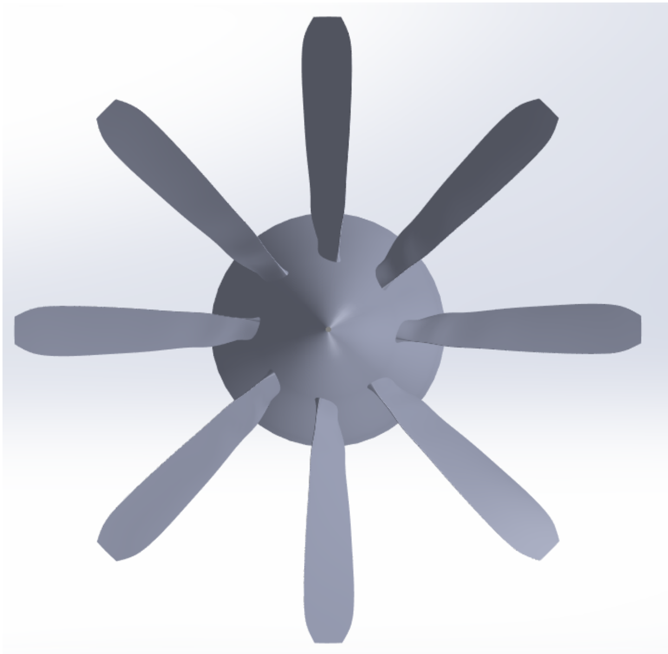

Figure 2.7: SR2 Propeller Front view

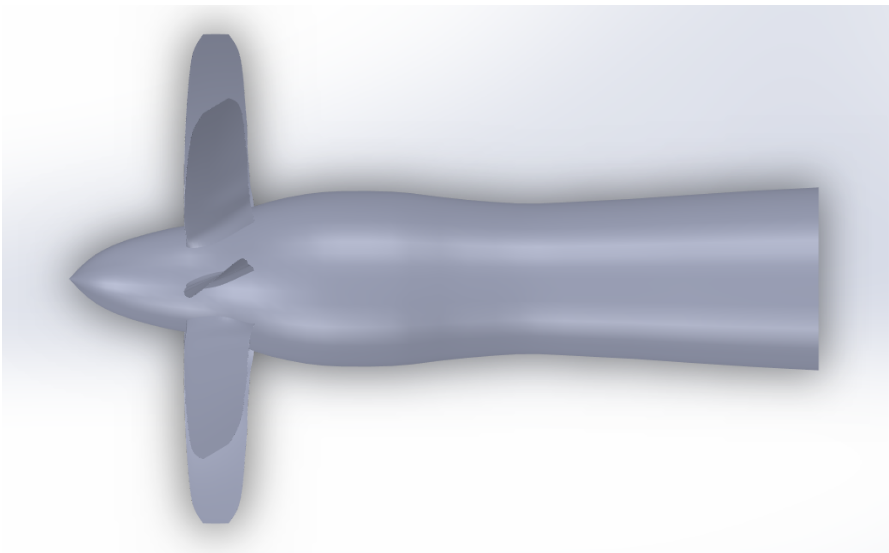

Figure 2.8: SR2 Propeller Side view

Once the blade is positioned, placing it in front of the nacelle (behind the spinner) results in the CP case (Conventional Propeller). Conversely, placing it behind the nacelle results in the BLI case (Boundary Layer Ingestion) propeller like is showed in figure 2.9

Figure 2.9: BLI propeller side view

2.3 Meshing and Preprocessing

2.3.1 Getting ready with the models

To speed up the calculations, we decided to use 1/8 of the propeller for both the CP and BLI cases, so each blade has an angular extension of $\frac{360°}{8} = 45°$. Figure 2.10 and Figure 2.11 show the segments of the CP and BLI blades used for the CFD analysis.

Figure 2.10: Segment of the CP blade

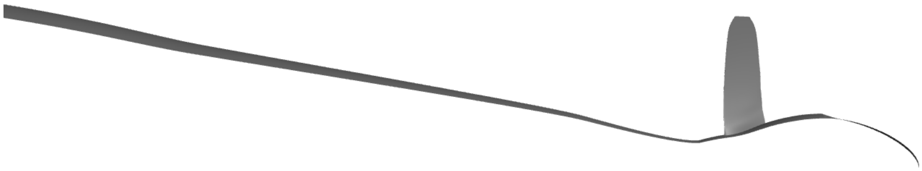

Figure 2.11: Segment of the BLI blade

Now, we need to build the mesh for both the stationary and rotor frames. In Figure 2.12 and Figure 2.13, we respectively show the boundaries of the stationary and rotating blocks. We apply the same procedure but with three different mesh accuracies to first validate the NASA data. In table 2.2 we show the meshes we build:

	Internal Block	External Block	Total cell Count
Coarse	939250	1299401	2238651
Medium	1573845	2391614	3965459
Fine	2601640	3756406	6358046

Table 2.2: Number of cells for the three meshes

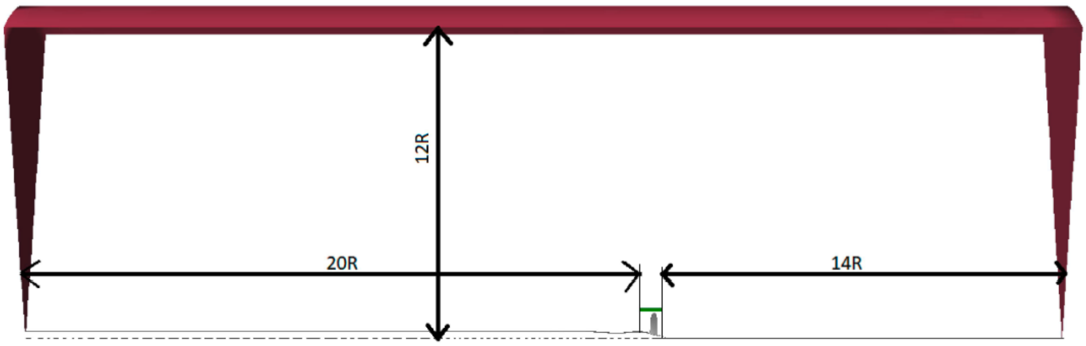

Figure 2.12: Stationary Domain dimensions

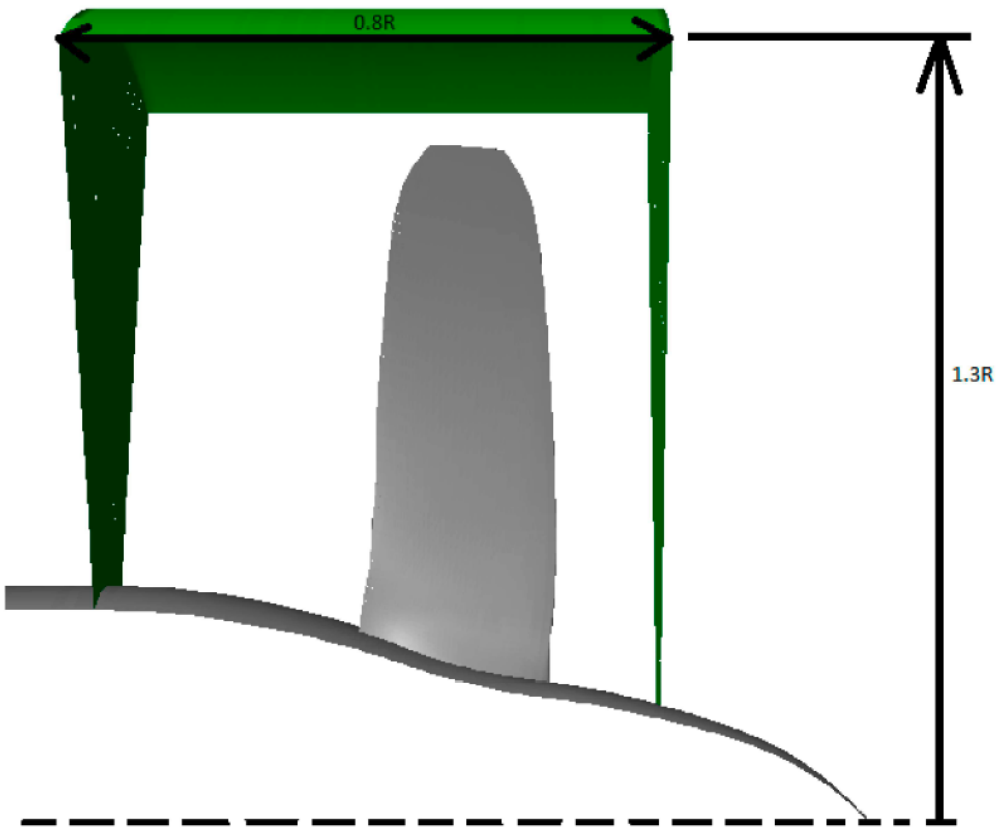

Figure 2.13: Rotational Domain dimensions

The Boundary condition to set up in Ansys Fluent[11] for the case are: (2.3)

Mach Flight Number	M=0.8
Altitude	h = 10660 [m]
Temperature	T=218.08 [K]
Density	$\rho = 0.378[\frac{Kg}{m^3}]$
β	56.7°

Table 2.3: Boundary Conditions set up

Once we defined the boundary conditions we launch the CFD simulation with the following parameters:

Parameter	Settings
Solution type	Density-based
Air density model	Ideal-gas
Turbulence	RANS k-ω
Viscosity Model	SSt
Solver Formulation	Implicit
Spatial discretization	First/second upwind
Time	Steady

Table 2.4: Caption for the table

2.4 Quality of results

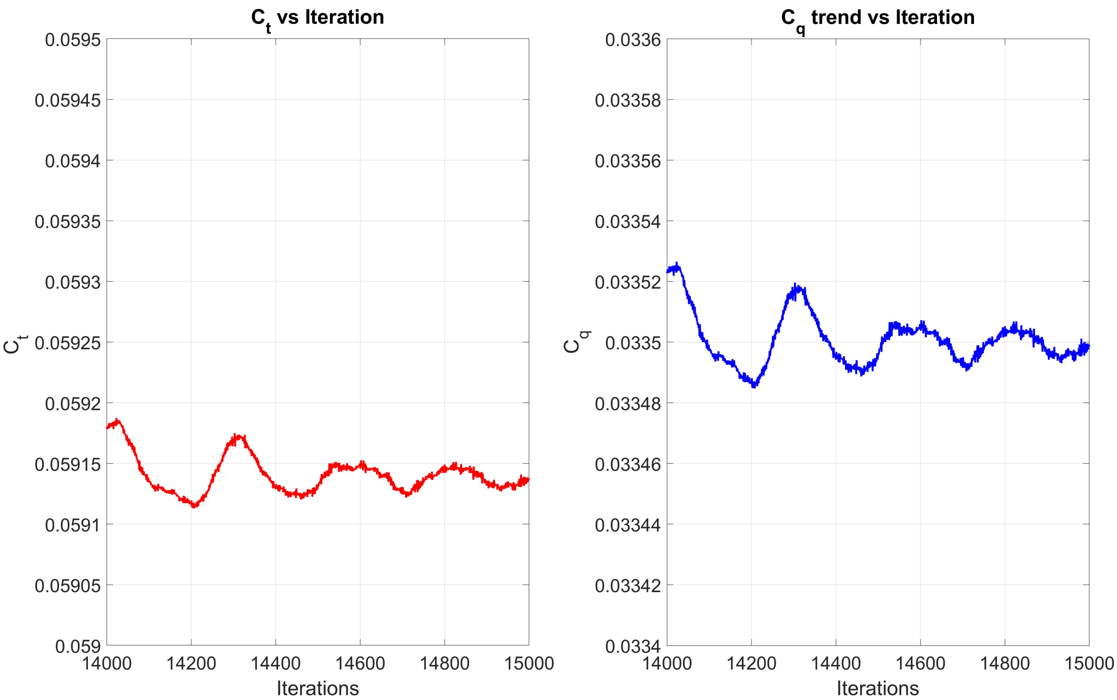

Figure 2.14: Convergence of Values of interest

In Figure 3.13, we illustrate the convergence of the last 1000 iterations of the relevant values to demonstrate the reliability of the results presented in the next chapter.

3 Results and discussion

In this chapter the main results obtained from the simulations are presented. In particular, we focus on the differences between the BLI case and the conventional propeller, showing first how the fluxes behave around the blade at different spans and continuing with the characteristic values of the propeller for the two cases. Finally, the comparison and contrast between the two propellers is discussed. All analyses are carried out with a constant pitch angle, that is, 56.7 ° at the 3/4 chord at different advance ratios.

3.1 NASA Data Validation

First of all, we compare our data, obtained through CFD, with the data obtained by NASA experimentally in a wind tunnel. To do so, we use the three meshes we prepared to analyze mesh sensitivity.In Figure 3.1, we plot the power coefficient as a function of the advance ratio J for the three meshes. Similarly, in Figure 3.2, we plot the thrust coefficient as a function of the advance ratio J for the three meshes.

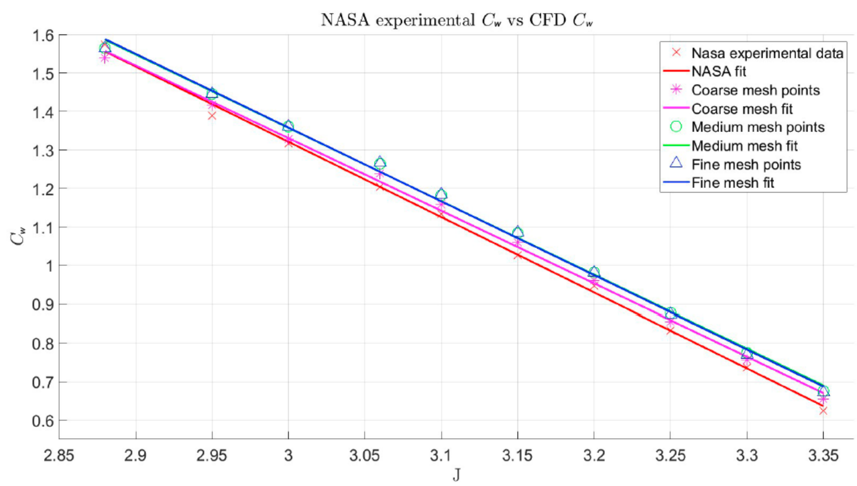

Figure 3.1: Mesh sensitivity Power Coefficient Cw

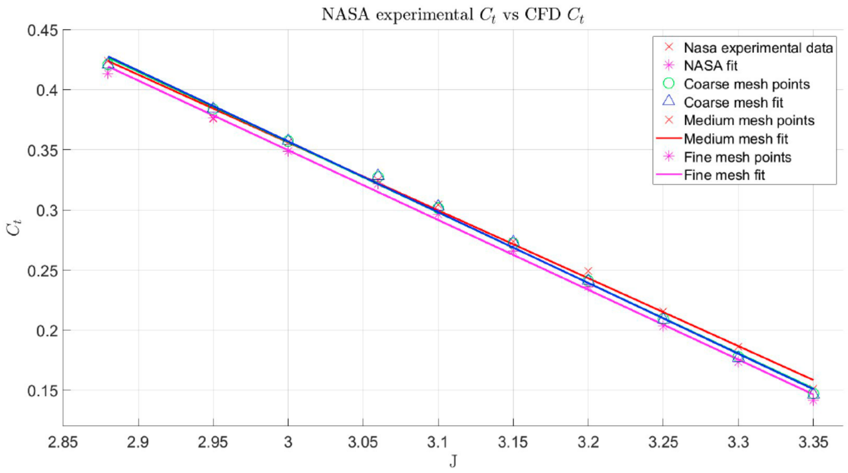

Figure 3.2: Mesh sensitivity Thrust Coefficient Ct

Instead in 3.3 and 3.4 we show the percentage error for both C_w and C_t.

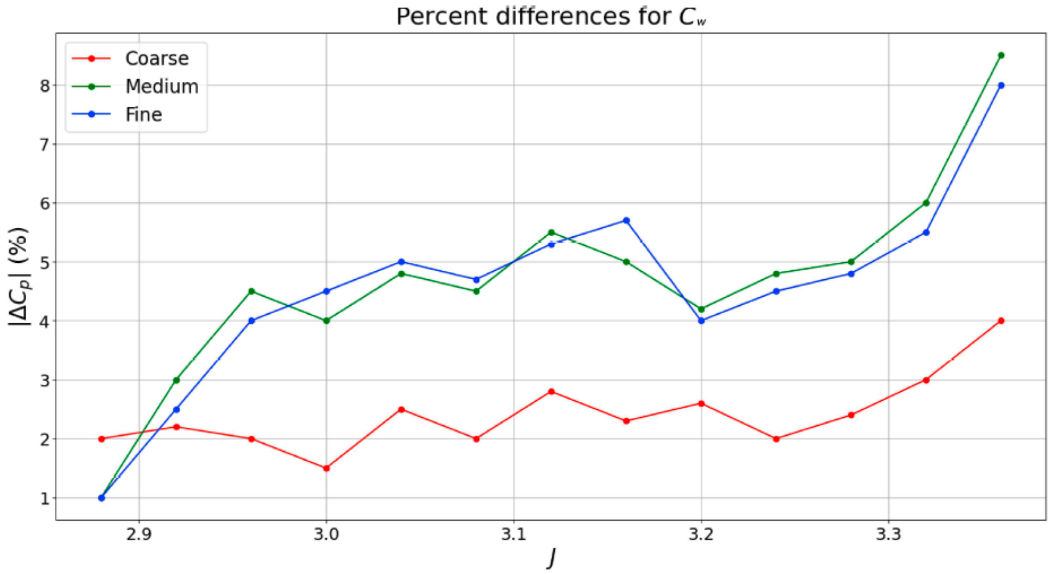

Figure 3.3: Percentage of error of C_w between CFD data and NASA data

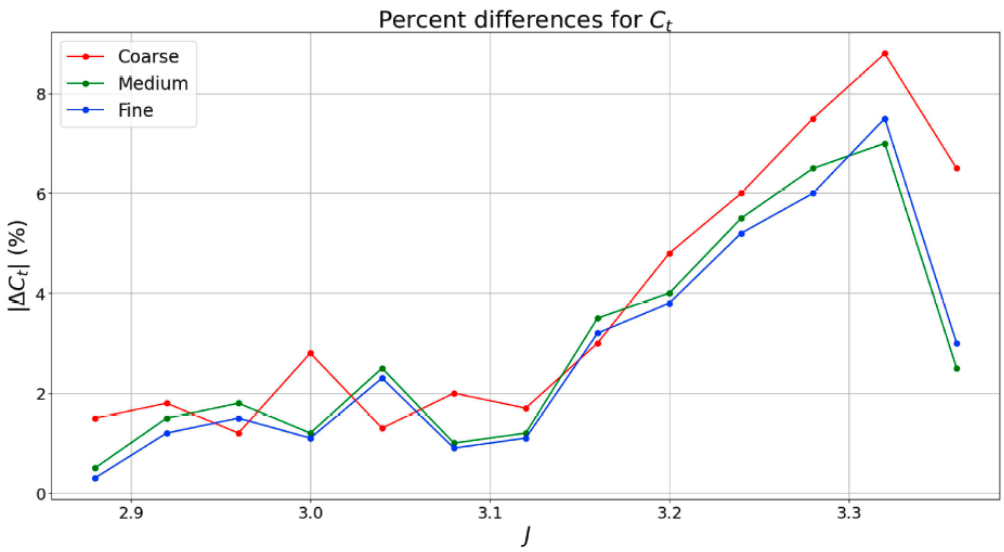

Figure 3.4: Percentage of error of C_t between CFD data and NASA data

From these graphs, it is possible to notice that, regarding C_w the lowest error occurs with the coarse mesh, while regarding C_t, the maximum error is about 8% with the coarse mesh. It is also important to note that the medium mesh provides the best overall results. This is because the coarse mesh yields the best results for C_w but the worst for C_t while the fine mesh performs best for C_t but worst for C_w.

3.2 Fluxes around the Blade

Figure 3.5 (a) shows the Mach number distribution and (b) illustrates the flow pattern around a near-root airfoil at J = 2.88 for the BLI configuration. In the same fashion, figure 3.6 shows the Mach contour and the streamlines for the CP case.

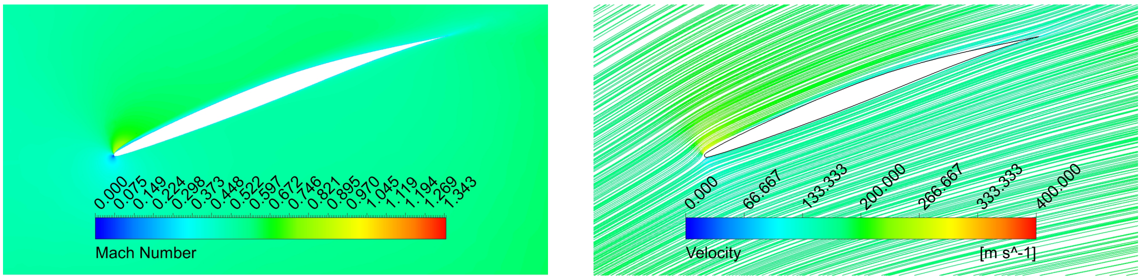

(a) Mach Contour

(b) Streamline

Figure 3.5: Trend of Mach number and streamlines around a near-hub airfoil for the BLI case at J=2.88.

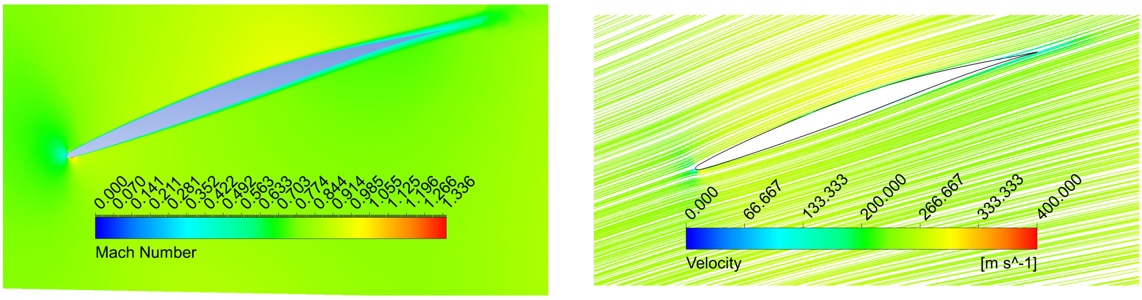

(a) Mach Contour

(b) Streamline

Figure 3.6: Trend of Mach number and streamlines around a near-hub airfoil for the CP case at J=2.88.

From image 3.5a and 3.6a is it possible to notice the difference between the two cases, in particular the BLI case shows a peak Mach number of M=0.6 whereas the CP case shows a peak of M=1.15, with an intense shock wave at the leading edge on the pressure side, and a weak one on the suction side. This is caused by the high speed of the fluid shown in 3.6b with a peak velocity of 334 m/s compared to 3.5b which shows a lower velocity in all the velocity field around the airfoil for the BLI case.

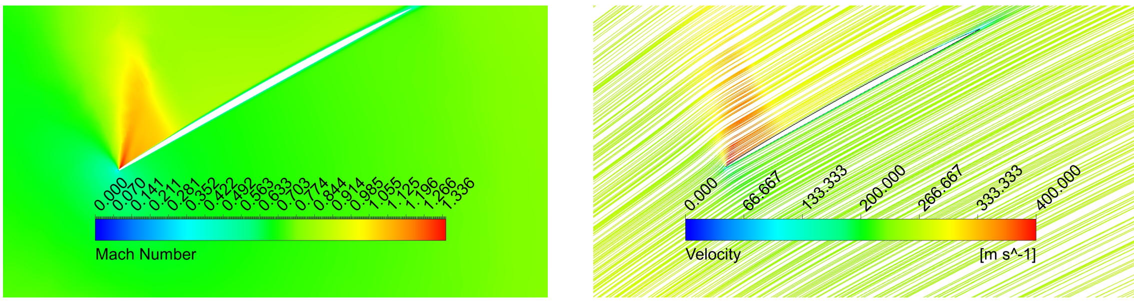

(a) Mach Contour

(b) Streamline

Figure 3.7: Trend of Mach number and streamlines at mid-span for the BLI case at J=2.88.

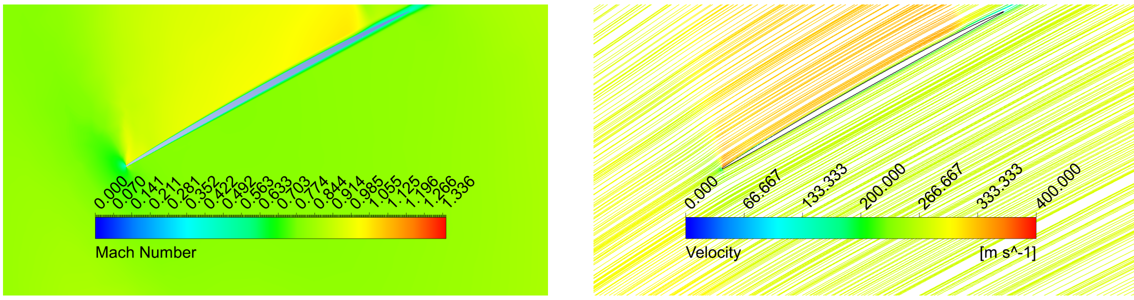

(a) Mach Contour (b) Streamline

Figure 3.8: Trend of Mach number and streamlines at mid-span for the CP case at J=2.88.

Analyzing the flow at mid-span instead, 3.7 and 3.8 highlight the difference: in fact, the BLI case exhibits a peak Mach number higher than that in the CP case, with a strong shock wave at the leading edge in the former, while in the latter, the strong shock wave appears at the trailing edge. It is also important to note that the flow in the CP case remains attached to the airfoil and never separates[12].

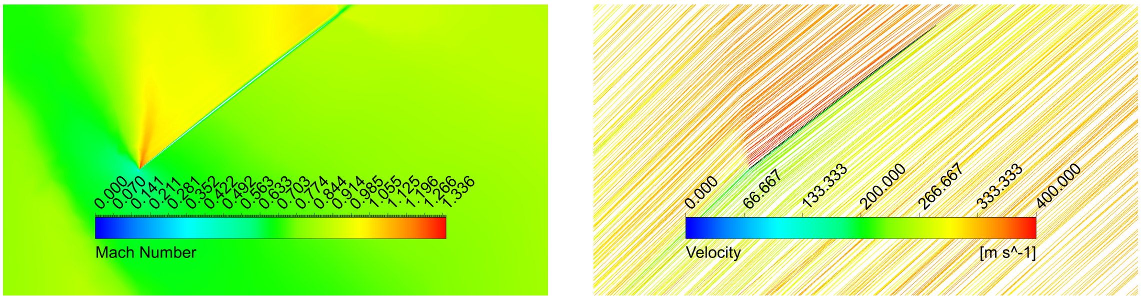

(a) Mach Contour (b) Streamline

Figure 3.9: Trend of Mach number and streamlines at near-tip for the BLI case at J=2.88.

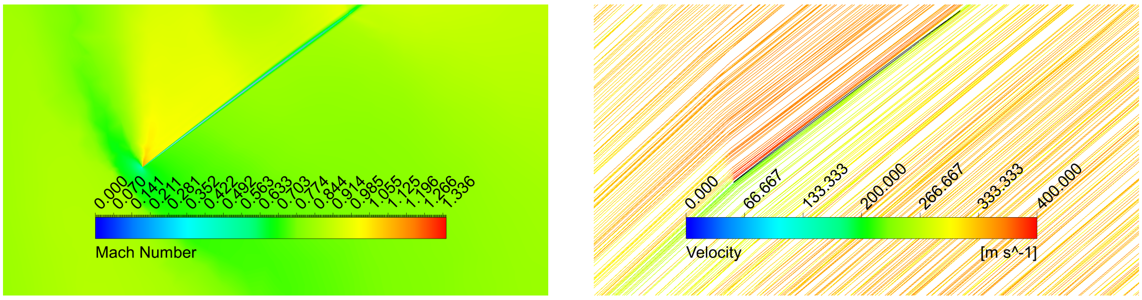

(a) Mach Contour (b) Streamline

Figure 3.10: Trend of Mach number and streamlines at near-tip for the CP case at J=2.88.

Finally, we focus in the near-tip airfoil: from 3.9 and 3.10: comparing the two cases, the BLI case shows a peak Mach number higher at the leading edge than the CP case, but in general shows a lower velocity of the flow around the blade than the CP case. To conclude, in figure 3.11 we show the tip vortex for both BLI and CP case.

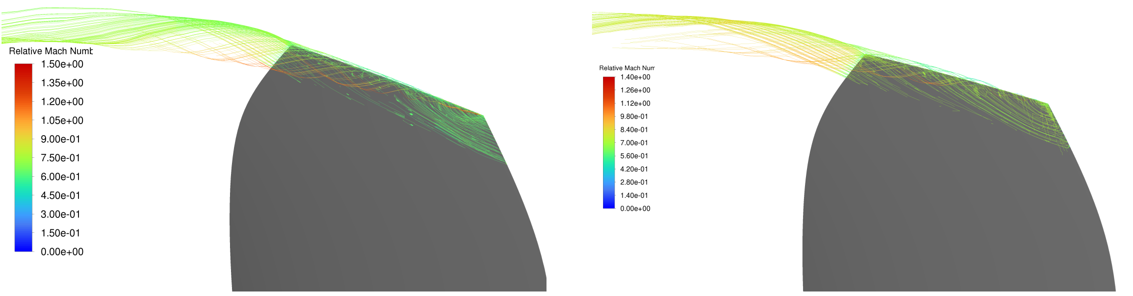

(a) Tip vortex BLI case (b) Tip vortex CP case

Figure 3.11: Tip vortex for the blade for both BLI and CP case

3.3 Coefficient and data

In this section, we present the data and the key coefficients that best characterize the aerodynamic and performance aspects of the blade. Specifically, we introduce the thrust coefficient, the power coefficient, and the efficiency parameter, which are fundamental in evaluating the blade's overall performance. Additionally, we analyze the pressure distribution along the blade, providing insights into the aerodynamic loads and their variation across its span. The selection and discussion of these coefficients aim to offer a comprehensive understanding of the blade's behavior, serving as a foundation for further analysis and potential design optimizations.

3.3.1 Efficiency

For the two cases analyzed, we show the efficiency η of the propeller as the advance ratio changes in 3.1 and 3.12.

J	2.88	2.95	3.00	3.06	3.20	3.30	3.35	3.45	3.60
η_{BLI}	0.809	0.826	0.838	0.854	0.884	0.896	0.902	0.905	0.887
η_{CP}	0.773	0.783	0.788	0.793	0.786	0.756	0.724	-	-

Table 3.1: Efficiency coefficients as a function of the advance ratio.

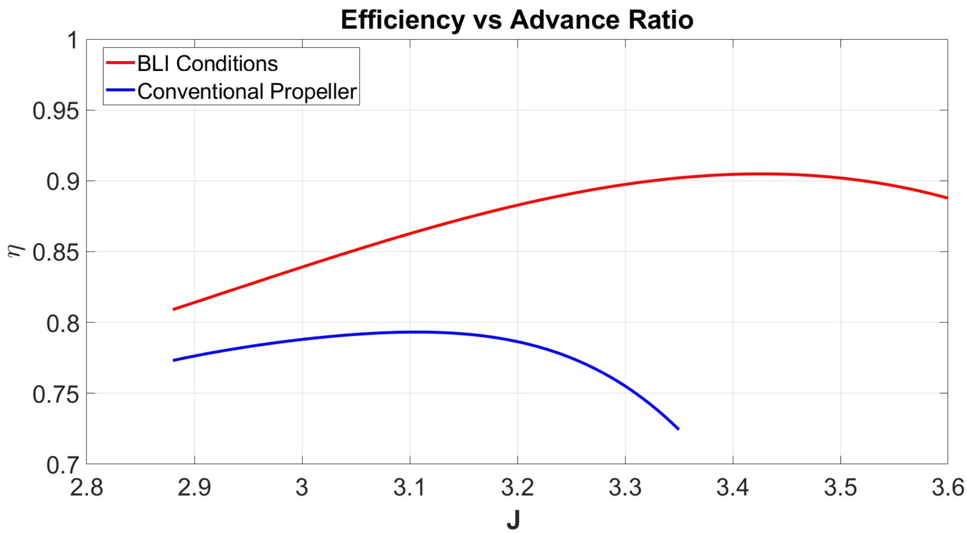

Figure 3.12: Efficiency vs Advance Ratio J

It can be observed from table 3.1 and 3.12 that the BLI case exhibits significantly higher efficiency compared to the CP case, along with a much broader operational range.Specifically, the graph clearly shows that the maximum operational advance ratio for the CP case is J=3.2,while for the BLI case, it reaches J=3.6. Furthermore, the advance ratio corresponding to maximum efficiency is $J^*_{BLI} = 3.425$ for the BLI case, whereas for the CP case it is $J^*_{CP} = 3.11$. The percentage increase by the BLI case respect the CP case is showed in table 3.2.

J	2.88	2.95	3.00	3.06	3.20	3.30	3.35
$\frac{BLI}{CP}$	+4.458%	+5.287%	+6.054%	+7.164%	+11.090%	+15.687%	+19.686%

Table 3.2: Percentage increase of BLI case respect CP case

3.3.2 Thrust Coefficient and Power Coefficient

Now we introduce the thrust coefficient C_t for both the cases in 3.3 and the image 3.13. In the same fashion we report the trend of the Power coefficient in 3.4 and 3.14.

J	2.88	2.95	3.00	3.06	3.20	3.30	3.35	3.45	3.60
C_t BLI	0.576	0.551	0.53	0.502	0.412	0.357	0.332	0.275	0.196
C_t CP	0.414	0.377	0.350	0.322	0.237	0.178	0.142	-	-

Table 3.3: Thrust coefficients for both cases vs J.

J	2.88	2.95	3.00	3.06	3.20	3.30	3.35	3.45	3.60
C_w BLI	2.059	1.979	1.911	1.808	1.499	1.323	1.240	1.053	0.799
C_w CP	1.539	1.417	1.327	1.239	0.961	0.756	0.655	-	-

Table 3.4: Power coefficients for both cases vs J.

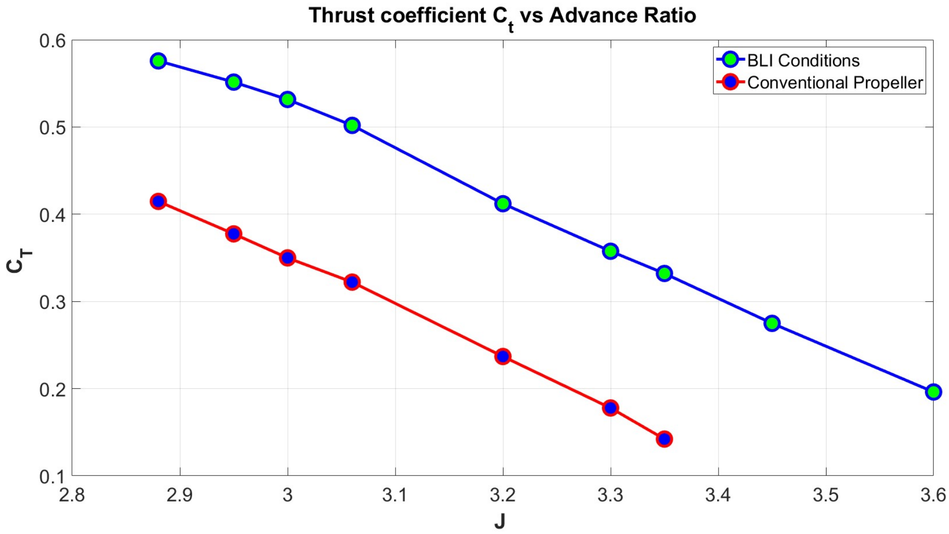

Figure 3.13: Thrust Coefficient vs Advance Ratio J

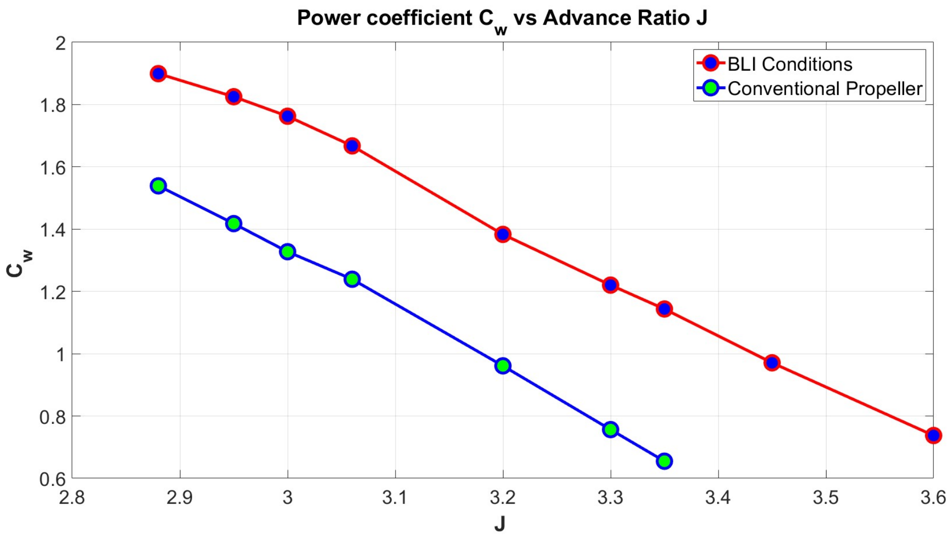

Figure 3.14: Power Coefficient vs Advance Ratio J

For both the cases, it is possible to observe that the BLI case has higher values respect the CP case: this means that the propeller in the BLI condition exerts more thrust respect the one in the CP condition, using more power to get that thrust. But since that:

$$\eta = J\frac{C_t}{C_w} \tag{3.1}$$

it means that in the BLI condition the thrust increase more than the power required to exhaust that thrust.

3.3.3 Pressure distribution along the blade

Now we discuss the Pressure distribution along the blade for the three advance ratio J=2.88/3.06/3.35 and we focus on the comparison between the BLI and CP case. The results are shown in 3.15, 3.16 and 3.17. As expected, for all the graph the max value of C_p is at the leading edge, and that's because we have a stagnation point.

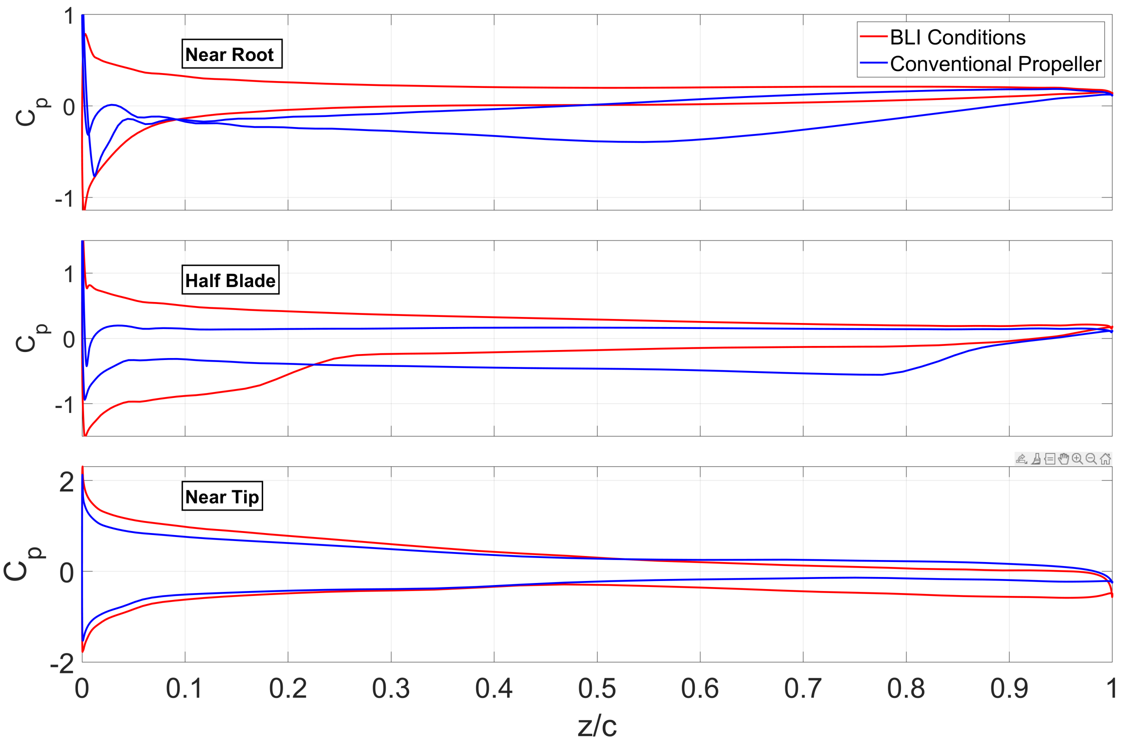

Figure 3.15: Pressure coefficient Cp J=288

In general we can notice that the C_p for the BLI case is smoother than C_p for the CP case, and that means:

- **Lower flow separation:** A smoother C_p could suggest that the flow remains more stable along the surface of the airfoil and that flow separation (which can cause spikes or oscillations in C_p is reduced.

- **Better pressure distribution:** A smoother C_p profile indicates that the pressure distribution along the BLI airfoil is more uniform. This could lead to reduced pressure peaks and, consequently, reduced stress and turbulence formation.

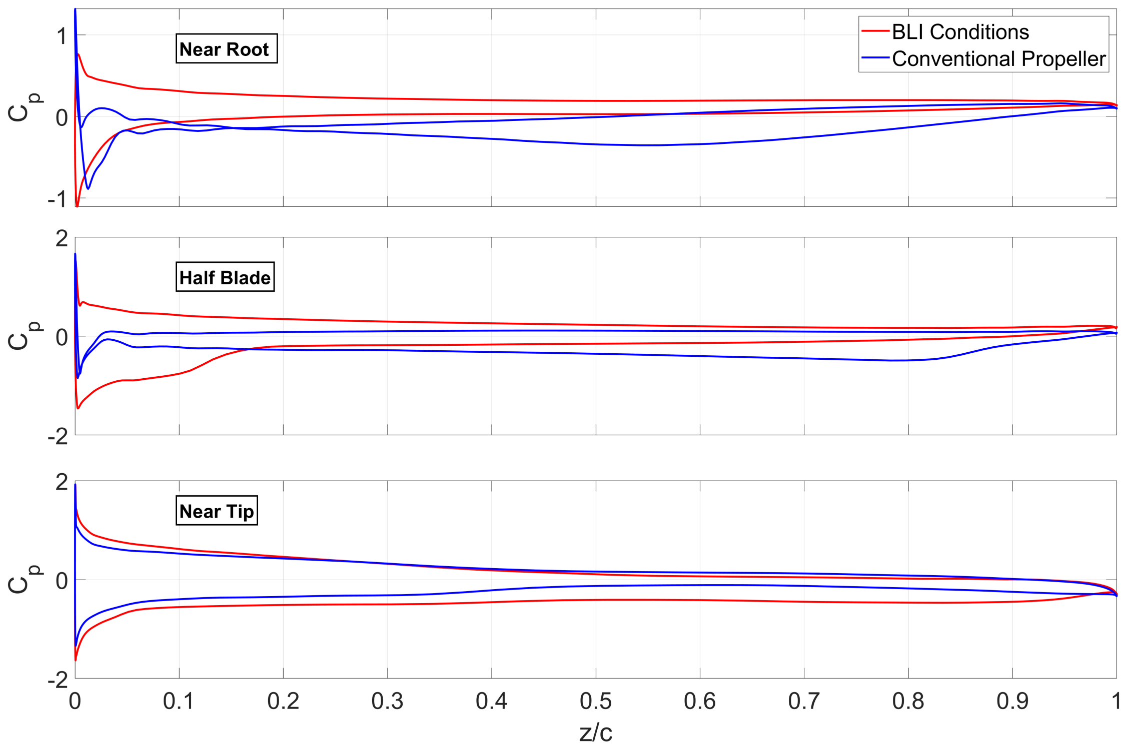

Figure 3.16: Pressure coefficient Cp J=306

Another observation is that the C_p increases as the advance ratio decreases, which can be attributed to the corresponding reduction in the velocity around the airfoil, as anticipated.

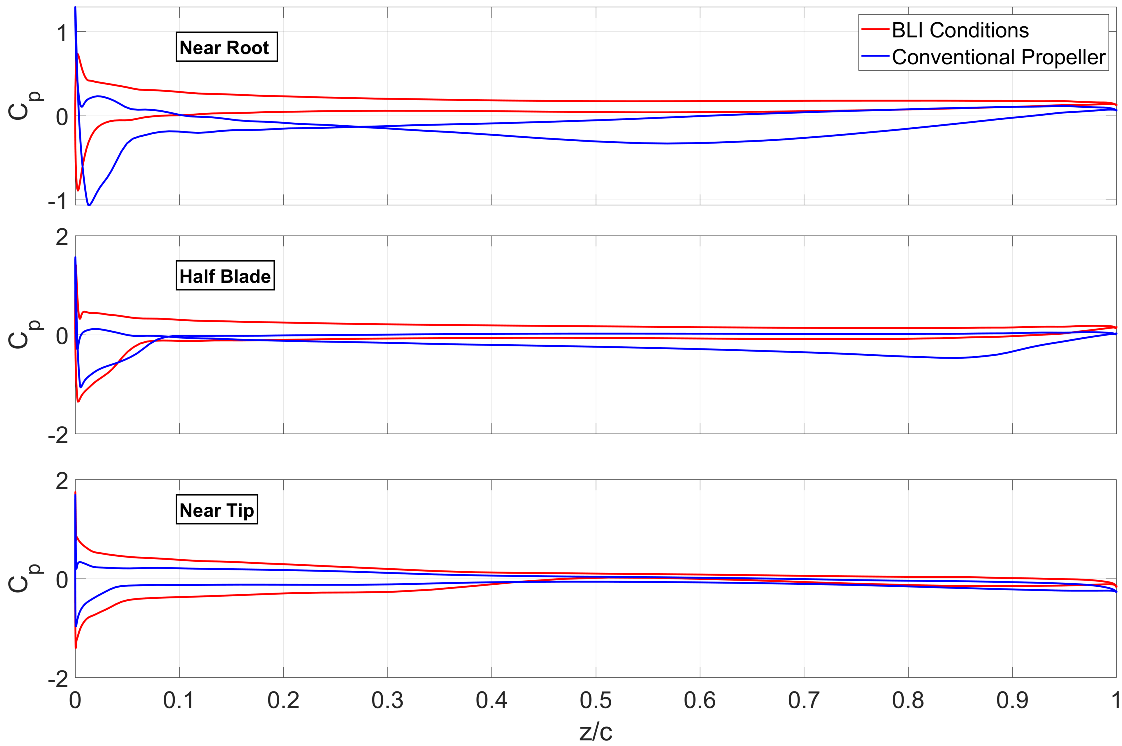

Figure 3.17: Pressure coefficient Cp J=335

3.3.4 Interaction between blade and flow

In the final section of this thesis, we analyze the interaction between the blade and the flow. The first analysis we present is the percentage of the total thrust force exerted at a given spanwise location relative to the total aerodynamic force generated by the entire blade for both cases BLI and CP. In figure 3.18, 3.20 and 3.20 we show the comparison:

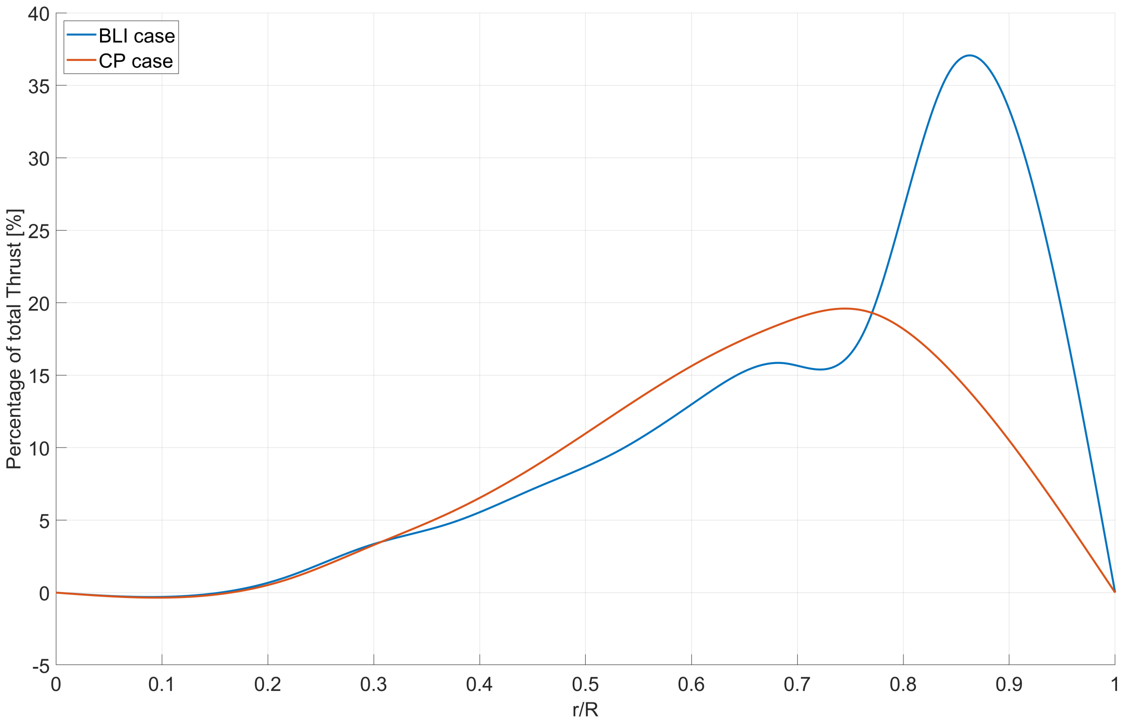

Figure 3.18: Percentage of Total Thrust along blade spanwise for J=2.88.

As shown above, the BLI case exhaust more than 50% from 0.75 and 1 of the span, meanwhile for the CP case the 50% is exhausted from 0.6 to 0.9, but in general the thrust is distributed along the span in a smoother way than the BLI case.

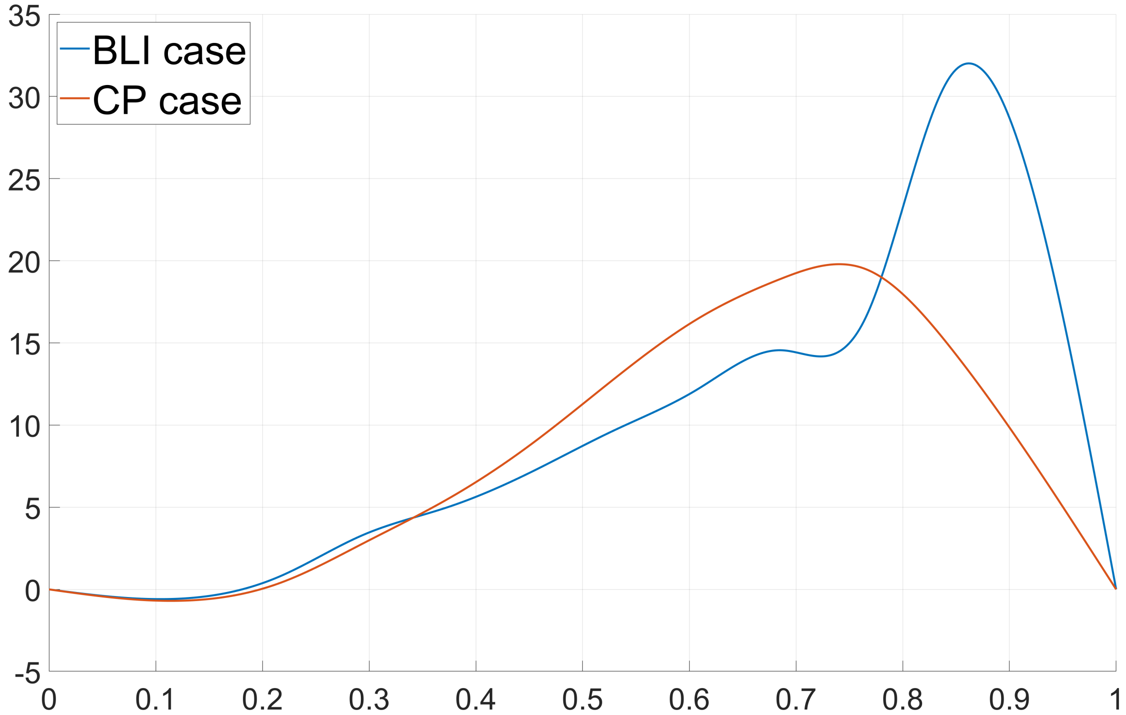

Figure 3.19: Percentage of Total Thrust along blade spanwise for J=3.06.

The trend for J=3.06 is almost the same than J=2.88 for the CP case, it is important to notice that for the BLI case the percentace of the peak is less than before, with a peak of 31%.

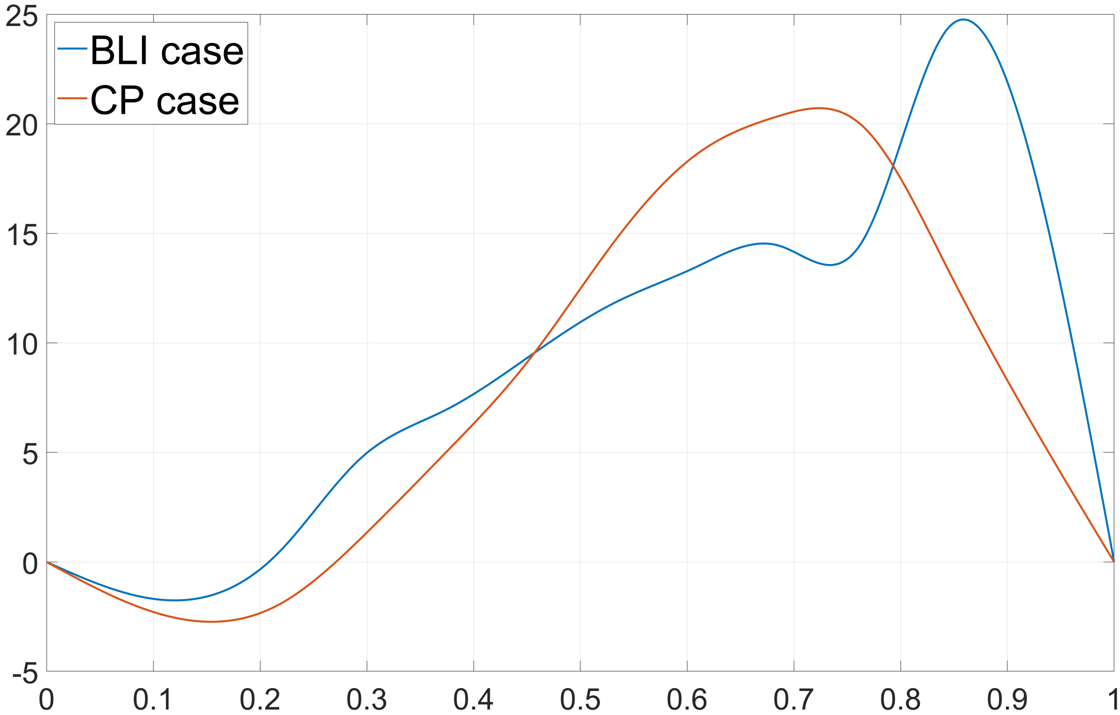

Figure 3.20: Percentage of Total Thrust along blade spanwise for J=3.35.

In the end we show the case of J=3.35: the CP case works in the same way of the previopus advance ratios, but the case of BLI propeller is still smoother, with a peak of 25%, and this means that to generate thrust all the blade works more than the previous case.

In general, the BLI case, exhibits a different distribution: from 0 to 0.4 span, the force distribution is similar to that of the CP case, but the majority of the force is generated from 0.8 span to the tip. This indicates that in the CP case, thrust is predominantly generated in the middle section of the blade, whereas in the BLI case, the final part of the blade contributes most significantly to thrust production. As the J values vary, the CP case appears to maintain a consistent trend across all three advance ratios, with only slight differences due to the relative flow velocity experienced by the blades. In contrast, the BLI j335 case shows a slightly different behavior, delivering a lower peak force at a span of 0.85 but slightly higher force at the blade center, between 0.25 and 0.65. In the end, it is essential to analyze the work exchanged with the air and identify which part of the blade is responsible for the highest energy transfer. To do so, we introduce the work coefficient ϕ:

$$\Psi = \frac{\Delta H_{tot}}{U_{tip}^2} = \frac{U_2 C_{U_2} - U_1 C_{U_1}}{U_{tip}^2} \tag{3.2}$$

which quantifies how much energy the blade transmits to the flow relative to its kinetic energy.

Figure 3.21, 3.22 and 3.23 present the results.

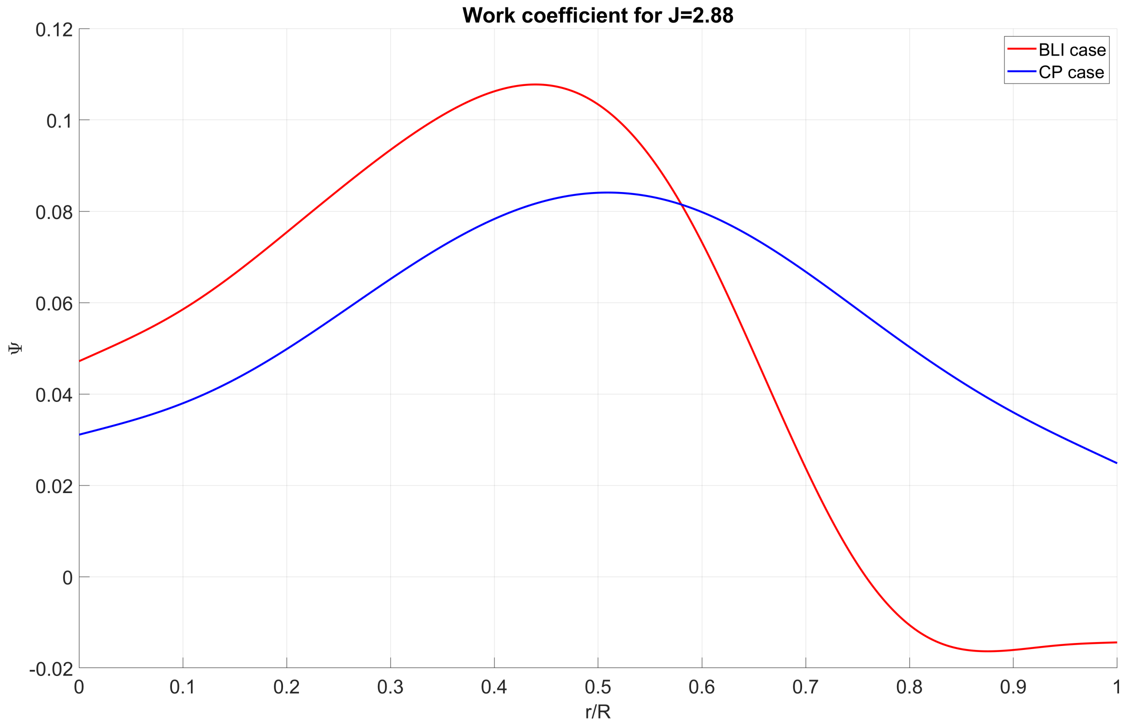

Figure 3.21: Work Coefficient Ψ vs normalized span for J=2.88

In particular, it is possible to notice that the work coefficient ψ decreases in both cases as J increases as it should be.

Figure 3.22: Work Coefficient Ψ vs normalized span for J=3.06

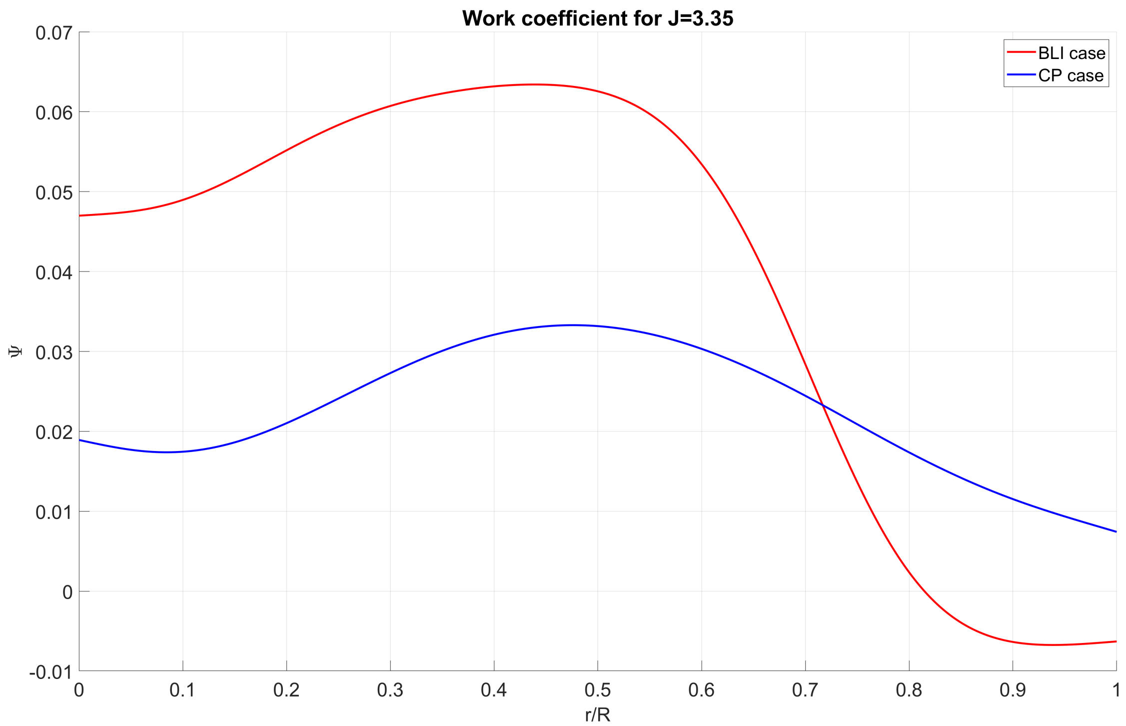

Figure 3.23: Work Coefficient Ψ vs normalized span for J=3.35

For J=2.88 the BLI case transfers more energy to the flow from 0 to approximately 0.59% of the span. Beyond this point, however, the CP case transmits more work to the fluid. For J=3.06 and J=3.35, the trend remains similar, with different spanwise locations where one case provides more work than the other. Specifically, for J=3.06 , this transition occurs at 0.69% of the span, while for J=3.35 , it occurs at 0.75%.

4 Conclusions

Based on the analyses performed on the NASA SR2 propeller CFD model, it was found that the BLI case is significantly more advantageous compared to the Cp case, both in terms of efficiency and thrust, which is much higher than in the Cp case. In particular, the BLI configuration achieves a maximum efficiency of approximately 91%, while the conventional configuration reaches a maximum of about 79%. Of course, many variables are involved: the type of fuselage used, flight speed, adopted advance ratio, etc. It should also be noted that in our CFD analyses, the aeroelastic effects of the structure were ignored, an aspect that could significantly influence the obtained results. Additionally, the type of solution we employed could lead to considerable variations in the results: for example, a transient solver might be more accurate than the frozen rotor model we used. Finally, an important aspect to consider is the quality of the mesh: for such complex geometries, it is extremely challenging to achieve a high-quality mesh that ensures the results are comparable to experimental data. A possible improvement for this thesis work could involve using a solver that does not rely on stationary models, as well as a finer discretization of the blade with a greater number of airfoils than the eleven we selected.

5 RIASSUNTO LAVORO DI TESI IN LINGUA ITALIANA

L'obiettivo di questa tesi è l'analisi e lo studio di un'elica ad alte prestazioni sviluppata dalla NASA alla fine degli anni '70, nota come NASA SR-2. In particolare, il presente lavoro si concentra sulla determinazione dei principali coefficienti aerodinamici, quali l'efficienza propulsiva η, il coefficiente di spinta C_te il coefficiente di potenza C_p, per due diverse configurazioni della stessa elica: la configurazione Conventional Propeller (CP), in cui l'elica è installata immediatamente dietro lo spinner, e la configurazione Boundary Layer Ingestion (BLI), in cui l'elica è posizionata dietro la fusoliera e opera all'interno dello strato limite del flusso. La prima fase dello studio ha riguardato un'analisi approfondita della letteratura scientifica pubblicata dalla NASA, finalizzata alla ricostruzione della geometria dell'elica. Dall'esame dei grafici prestazionali disponibili, è stato possibile determinare che la pala impiega profili aerodinamici NACA 65 nella regione dell'hub fino a circa il 37% dell'apertura, mentre dal 44% dello span fino all'estremità (tip) adotta profili NACA 16. Per identificare con precisione i profili effettivamente utilizzati lungo l'apertura, è stato impiegato un codice di validazione basato sulla Blade Element Momentum Theory (BEMT), il quale ha consentito di confrontare le polari aerodinamiche fornite dalla NASA con quelle ottenute dalle simulazioni. Una volta definita con accuratezza la distribuzione dei profili lungo la pala, è stata realizzata la modellazione tridimensionale mediante il software CAD SolidWorks. In seguito, il modello è stato implementato in Ansys Fluent per l'analisi CFD delle due configurazioni, CP e BLI. La tecnica di simulazione adottata è stata quella del Moving Reference Frame (MRF) basata sul metodo Frozen Rotor. Le simulazioni sono state condotte in regime stazionario, impiegando il modello di turbolenza $k - \omega SST$ con aria trattata come gas ideale. Le condizioni al contorno considerate comprendono un numero di Mach pari a $M = 0.8$ e una quota di volo di $h = 10660m$ mentre i restanti parametri sono stati determinati tramite le equazioni dell'atmosfera standard ISA.I risultati ottenuti hanno confermato, con scarti di errore ridotti, la validità dei dati sperimentali forniti dalla NASA. Inoltre, è emerso che la configurazione BLI offre un'efficienza significativamente superiore rispetto alla configurazione CP, con un valore di circa 91%, rispetto al 79% riscontrato nel caso CP.

BIBLIOGRAPHY

[1] Roy D. Hager, Deborah Vrabel, "Advanced turboprop projects," 1986.

[2] J. D. Anderson, *Aircraft Performance and Design*. McGraw-Hill, 2010.

[3] F. Costa, J. Tomita, V. Silva, N. Andersson, T. Gronstedt, and C. Bringhenti, "Aerodynamic analysis of conventional and boundary layer ingesting propellers," *Journal of Engineering for Gas Turbines and Power*, vol. 145, 07 2022.

[4] U.S. Department of Transportation, Federal Aviation Administration, Flight Standards Service l, "Aviation handbooks manuals," 2003.

[5] A. El-Sayed, *Aircraft Propulsion and gas turbine engines*. CRC Press, 2008.

[6] "Plot digitizer." https://plotdigitizer.com/.

[7] Stefko, George L.,Jeracki, Robert J, "Wind-tunnel results of advanced high-speed propellers at takeoff, climb, and landing mach numbers," 1985/11.

[8] L. Joseph Herrig,JamesC.Emery,JohnR.Erwin,, "Systematictwo-dimensionalnaca65-seriescompressor bladescascadeat-lowspeed,technicalnote3916,," 1957.

[9] "Xfoil." https://web.mit.edu/drela/Public/web/xfoil//.

[10] "Guida dello studente per l'apprendimento del software solidworks." https://www.solidworks.com/sw/docs/student_wb_2011_ita.pdf//.

[11] "Ansysfluentuser'sguide." https://www.afs.enea.it/project/neptunius/docs/fluent/html/ug/main_pre.htm.//.

[12] S. Gudmundsson, *General Aviation Aircraft Design*. butterworth heinemann, 2013.

ACKNOWLEDGEMENT

I would like to express my gratitude to my supervisor and co-supervisor for their professionalism, precision, and punctuality in guiding me throughout this thesis work. Finally, I would like to thank my university friends, who made every class day enjoyable and carefree.